SUPPORTING INFORMATION

Tissue size controls patterns of cell proliferation and migration in freely-expanding epithelia

Matthew A. Heinrich[a], Julienne M. LaChance[a], Tom J. Zajdel[a], Ricard Alert[b,c], Andrej Košmrlj[a,d], Daniel J. Cohen[a*]

[a]Department of Mechanical and Aerospace Engineering, Princeton University, Princeton, NJ 08544

[b]Lewis-Sigler Institute for Integrative Genomics, Princeton University, Princeton, New Jersey 08544, USA

[c]Princeton Center for Theoretical Science, Princeton University, Princeton, New Jersey 08544, USA

[d]Princeton Institute for the Science and Technology of Materials (PRISM), Princeton University, Princeton, New Jersey 08544, USA

*corresponding authors

Daniel J. Cohen (danielcohen@princeton.edu)

Table of contents

1. Supplementary Methods

Cell Culture. All experiments were performed with MDCK-II cells expressing the FUCCI cell-cycle marker system (1). We cultured cells in customized media consisting of low-glucose (1 g/L) DMEM with phenol red (Gibco, USA), 1 g/L sodium bicarbonate, 1% streptomycin/penicillin, and 10% FBS (Atlanta Biological, USA). Cells were maintained at 37 °C and 5% CO2 in humidified air.

Tissue Patterning. We coated tissue-culture plastic dishes (BD Falcon, USA) with type-IV collagen (MilliporeSigma, USA) by incubating 150 µL of 50 µg/mL collagen on the dish under a glass coverslip for 30 minutes at 37°C, washing 3 times with deionized distilled water (DI), and allowing the dish to air-dry. We then fabricated silicone stencils with cutouts of desired shape and size and transferred the stencils to the collagen coated surface of the dishes. Stencils were cut from 250 μm thick silicone (Bisco HT-6240, Stockwell Elastomers) using a Silhouette Cameo vinyl cutter (Silhouette, USA). We then seeded the individual stencils with cells suspended in media at ~1000 cells/mL. Suspended cells were concentrated at ~2.25×10^6 cells/mL and pipetted into the stencils at the appropriate volume. Care was taken not to disturb the collagen coating with the pipette tip. To allow attachment of cells to the collagen matrix, we incubated the cells in the stencils for 30 minutes in a humidified chamber before flooding the dish with media. We then incubated the cells for an additional 18 hours to allow the cells to form monolayers in the stencils, after which the stencils were removed with tweezers. Imaging began ~30 minutes after stencil removal. Media without phenol red was used throughout seeding and imaging to reduce background signal during fluorescence imaging.

Live-cell Time-lapse Imaging. All imaging was performed with a 4X phase contrast objective on an automated, inverted Nikon Ti2 with environmental control (37 °C and humidified 5% CO2) using NIS Elements software and a Nikon Qi2 CMOS camera. Phase contrast images were captured every 20 minutes, while RFP/GFP channels were captured every 60 minutes at 25% lamp power (Sola SE, Lumencor, USA) and 500 ms exposure time. No phototoxicity was observed under these conditions for up to 48 hrs. Final images were composited from 4x4 montages of each dish using NIS Elements.

Tissue Growth Analysis. Tissues were segmented to make binary masks using a custom MATLAB (Mathworks) script. Edge radial velocity was calculated for each timepoint as the rate of change of the average extent of the boundary pixels of the tissue mask. Data shown utilized a rolling average of 3 timepoints (1 hr) to account for capture phase offsets resulting from capturing phase and fluorescence images at different frequencies.

Cell Counts. The FUCCI system contains a period after M-phase where cells go dark, making FUCCI unreliable for cell counting. Instead, we developed and trained a convolutional neural network to reproduce nuclei from 4X phase contrast images. The output of this neural network was then segmented in ImageJ to determine nuclei footprints and centroids.

Tissue Local Migration Velocity and Density measurements. We preprocessed the image sequences in MATLAB to subtract the background and resized the images to reduce the number of pixels by a factor of 2 in each dimension. Resizing was performed with bicubic interpolation and antialiasing. Tissue velocity vector fields were calculated from phase contrast image sequences using the free MATLAB package PIVLab (2) with the FFT window deformation algorithm. We used a 1st pass window size of 64×64 pixels with 32 pixel overlap and second pass of 32×32 pixels with 50% pixel overlaps. This resulted in a ~115×115 µm window, containing ~30 cells at the start of experiments. Local density was also calculated for each PIV window by counting the number of approximate nucleus centroids in that window. Speed data from PIV was smoothed in time with a moving average of 3 timepoints centered at each timepoint as before.

Kymographs of Speed, Density, and Vorticity. First, we constructed kymographs for each given metric for each tissue using only measurements that took place within the tissue footprint. To this end, we found the average local measurement at each timepoint and within annuli of width equal to 1 PIV window width (or 1 pixel after PIV analysis). We removed kymograph pixels for which at least 95% of the possible measurement locations within the corresponding annulus were located outside of the tissue footprint. For the average kymographs displayed in the main figures, we averaged the corresponding tissue kymographs together, ignoring removed pixels.

Trajectory colorization. We first generated a plot of all relevant trajectories (3) colorized randomly in grayscale using a custom MATLAB (Mathworks) script. We then used the Fiji plugin OrientationJ on this plot to colorize the resulting composite image according to orientation (4).

Cell displacement definitions. For cell displacements of the small tissue vortex, we selected the 24-42 h period of trajectories spanning at least that period. We defined radial displacement Rad_i for each trajectory *i* as:

$$\mathrm{Rad}_i = r_{i,t_{42}} - r_{i,t_{24}},$$

Where r_i is the distance from the center of a trajectory, t_{42} is 42 h and t_{24} is 24 h.

We defined angular displacement $\mathrm{Ang_i}$ similarly as:

$$\mathrm{Ang_i} = \theta_{i,t_{42}} - \theta_{i,t_{24}},$$

Where θ_i corresponds to the angular location of a cell.

We defined tangential displacement Tan_i by integrating the tangential component of the trajectory velocity over the course of the trajectory:

$$\mathrm{Tan}_i = \int_{t=t_{24}}^{t_{42}} \left|\boldsymbol{v_{i,t}}\right| \cos\left(\theta_{i,t}\right) dt$$

Cell Density Simulation. To test whether the observed spatiotemporal evolution of density $\rho(r,t)$ could be explained by flow of material (rather than divisions, extrusions, and cell death), we solved the continuity equation for a homogenous tissue in a circular geometry with spatiotemporal evolution of radial velocity $v_r(r,t)$ as measured from PIV in experiments. The continuity equation is

$$\frac{\partial \rho}{\partial t} = -\nabla \cdot \boldsymbol{j} + k_0 \rho, \qquad \text{(S1)}$$

where a homogeneous cell proliferation rate $k_0 = 1.04\ \mathrm{h}^{-1}$ is assumed throughout the tissue, which corresponds to the cell doubling time of 16h. The current density is $\boldsymbol{j} = \rho \boldsymbol{v_r} - \mathrm{D}\nabla\rho$, where we included a diffusion term with a small diffusion constant $D = 0.22 \frac{mm^2}{h}$ for numerical stability.

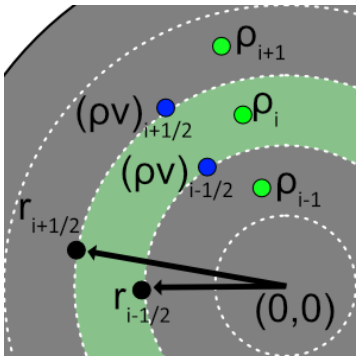

The continuity equation (S1) was discretized using the finite volume method, which is briefly summarized below. As shown on the schematic image on the right, the tissue domain was divided into an inner circle Ω_0 of radius $r_{1/2} = \frac{1}{2}\Delta r$ and circular annuli Ω_i with inner radii $r_{i-1/2} = \left(i - \frac{1}{2}\right)\Delta r$ and outer radii $r_{i+1/2} = \left(i + \frac{1}{2}\right)\Delta r$, respectively, where $i = 1,2,3,\ldots$ and $\Delta r = 115\mu m$ corresponds to the width of 1 window in the PIV analysis. The continuity Equation (S1) was then integrated over the inner circle Ω_0 and circular annuli Ω_i as

$$\frac{1}{A_0}\int_{r_0}^{r_{1/2}} (2\pi r dr)\frac{\partial \rho}{\partial t} = \frac{1}{A_0}\int_{r_0}^{r_{1/2}} (2\pi r dr)\left[-\nabla \cdot \boldsymbol{j} + k_0\rho\right], \qquad \text{(S2a)}$$

$$\frac{1}{A_i}\int_{r_{i-1/2}}^{r_{i+1/2}} (2\pi r dr)\frac{\partial \rho}{\partial t} = \frac{1}{A_i}\int_{r_{i-1/2}}^{r_{i+1/2}} (2\pi r dr)\left[-\nabla \cdot \boldsymbol{j} + k_0\rho\right], \qquad \text{(S2b)}$$

where $A_0 = \pi r_{1/2}^2$ is the area of the inner circle Ω_0 and $A_i = \pi r_{i+1/2}^2 - \pi r_{i-1/2}^2$ are the areas of the circular annuli Ω_i. The integrals in Equation (S2) can be approximated as

$$\frac{\partial \rho(0,t)}{\partial t} = -\frac{2\pi}{A_0} r_{1/2} j\left(r_{1/2}, t\right) + k_0 \rho(0,t), \quad \text{(S3a)}$$

$$\frac{\partial \rho(r_i,t)}{\partial t} = -\frac{2\pi}{A_0}\left[r_{i+1/2} j\left(r_{i+1/2}, t\right) - r_{i-1/2} j\left(r_{i-1/2}, t\right)\right] + k_0 \rho(r_i,t). \quad \text{(S3b)}$$

Here, density profiles $\rho(r_i,t)$ are evaluated at $r_i = i\Delta r$ for all $i = 0,1,2,\ldots$ Current densities are evaluated as $j\left(r_{i+\frac{1}{2}},t\right) = \rho\left(r_{i+\frac{1}{2}},t\right) v_r\left(r_{i+\frac{1}{2}},t\right) - D[\rho(r_{i+1},t) - \rho(r_i,t)]/\Delta r$ for all $i = 0,1,2,\ldots$, where $\rho\left(r_{i+\frac{1}{2}},t\right) = [\rho(r_i,t) + \rho(r_{i+1},t)]/2$ and $v_r\left(r_{i+\frac{1}{2}},t\right) = [v_r(r_i,t) + v_r(r_{i+1},t)]/2$. Density profiles $\rho(r_i,t)$ were then obtained by integrating Equations (S3) with the forward Euler method using a time step $\Delta t = 20$ min to align with experimental data collection of radial velocity profiles $v_r(r_i,t)$. The initial conditions were $\rho(r_i,0) = 2700$ cells/mm^2 for $r_i < r_{tissue}$ and $\rho(r_i,0) =$ 0cells/mm^2 for $r_i > r_{tissue}$, where r_{tissue} is the radius of tissue at the beginning of experiment. For comparison with experimental data (see Fig. 4 in the main text), we thresholded the kymographs of simulated density at 100 cells/mm^2, which corresponds to much lower density than a confluent tissue.

Cell Cycle Analysis. The Fucci system consists of an RFP and GFP fused to proteins Cdt1 and Geminin, respectively (5). Cdt1 levels are high during G1 and low during the rest of the cell cycle, while Geminin levels are high during the S, G_2, and M phases (1, 5). After capturing the appropriate fluorescence images, preprocessing was implemented identically for GFP and RFP channels. Background subtraction and histogram normalization with 0.3% saturated pixels were performed on images from single time-points in ImageJ to normalize RFP and GFP channels. To determine local cell cycle fraction, we utilized the previously described dataset of nuclei footprints to determine the median value of RFP and GFP signal for each cell nucleus. We manually selected thresholds for RFP and GFP signals separately for each independent experiment and classified cell cycle for each cell as G0-G1-S (RFP above threshold), S-G2-M (RFP below threshold and GFP above threshold), or postmitotic (RFP and GFP below threshold). Local cell cycle fraction of each state could then be easily computed for each PIV pixel. Note that S phase (both RFP and GFP signals above threshold) did not prove to be a useful or reliable feature for segmentation.

2. Supplementary Figures and Captions

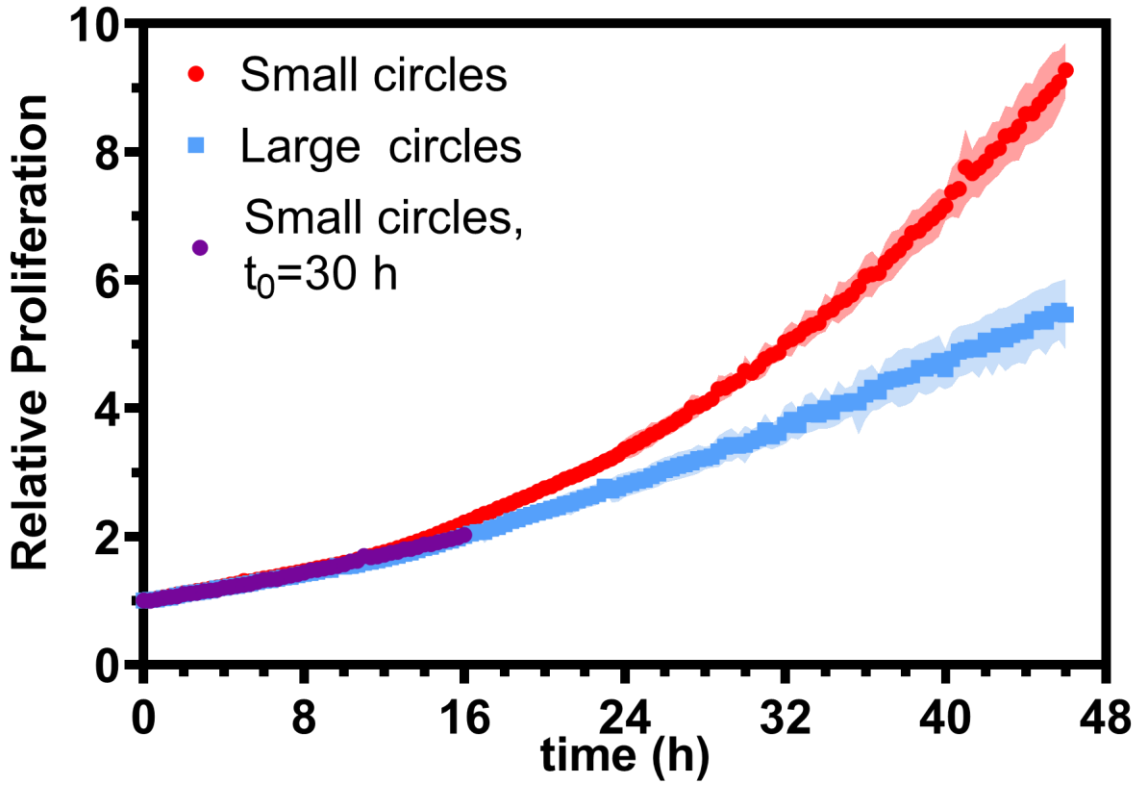

Figure S1. Relative cell number $N(t)/N_0$ for small and large tissues, where N_0 and N(t) are the numbers of cells at the beginning of the experiment and at time t, respectively. Purple points show the relative area increase, $A(t+t_0)/A(t_0)$, of small tissues from the time t_0=30h when they reached the starting size of the large circles.

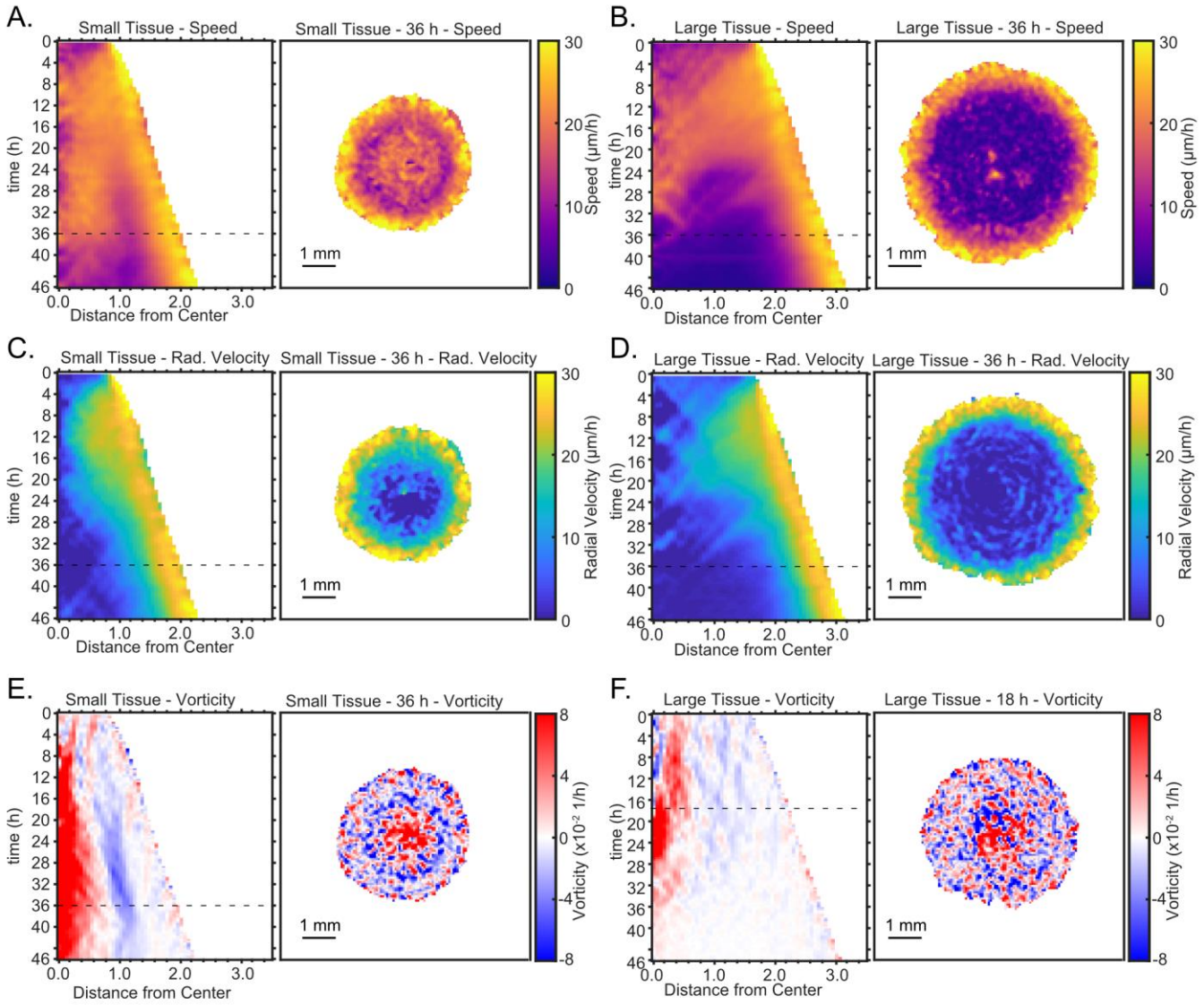

Figure S2. Representative kymographs and heatmaps for speed (A-B), radial velocity (C-D), and vorticity (E-F). Dashed lines indicate timepoint to which heatmaps correspond. Kymographs and heatmaps in each column are from the same representative tissue. Note that the snapshot in F is taken from 18 h instead of 36 h to include the time of high vorticity at that earlier timepoint relative to 36 h.

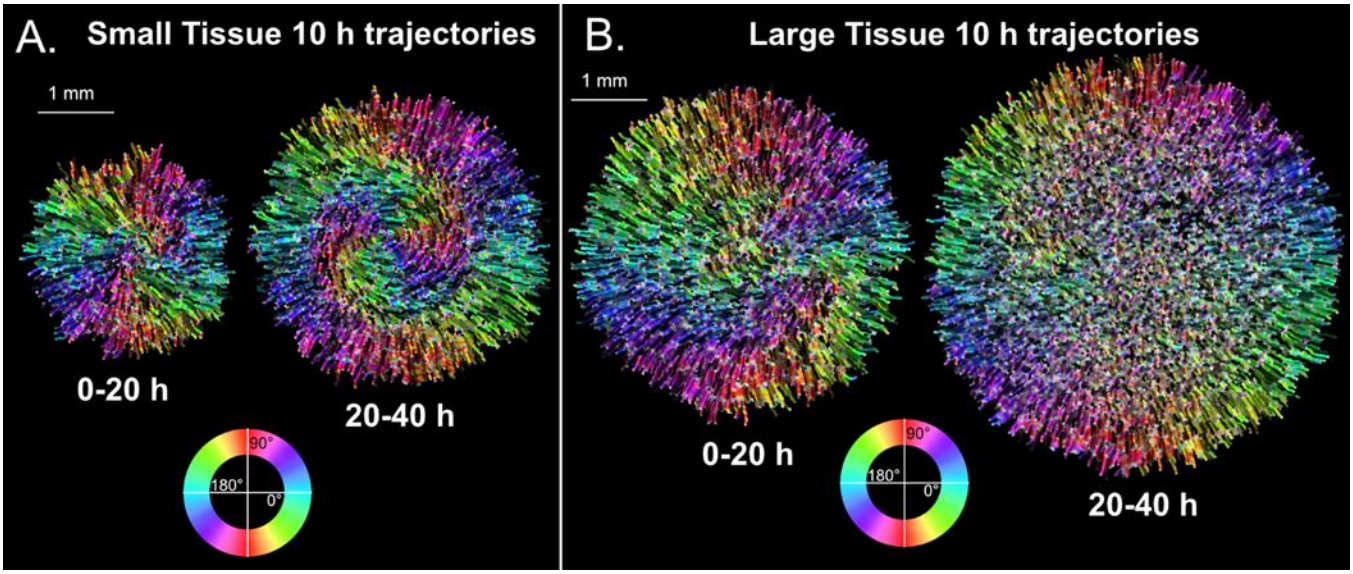

Figure S3. (A) 10 h trajectories in a representative small tissue colored by orientation from 0-20 h (left) and 20-40 h (right). Note the strong vortex during 20-40 h. (B) 10 h trajectories in a representative large tissue colorized by orientation from 0-20 h (left) and 20-40 h (right). A vortex can be identified in the center-right region during 0-20 h, but no vortex is present during 20-40 h as most trajectories in the center of the tissue only include small distances.

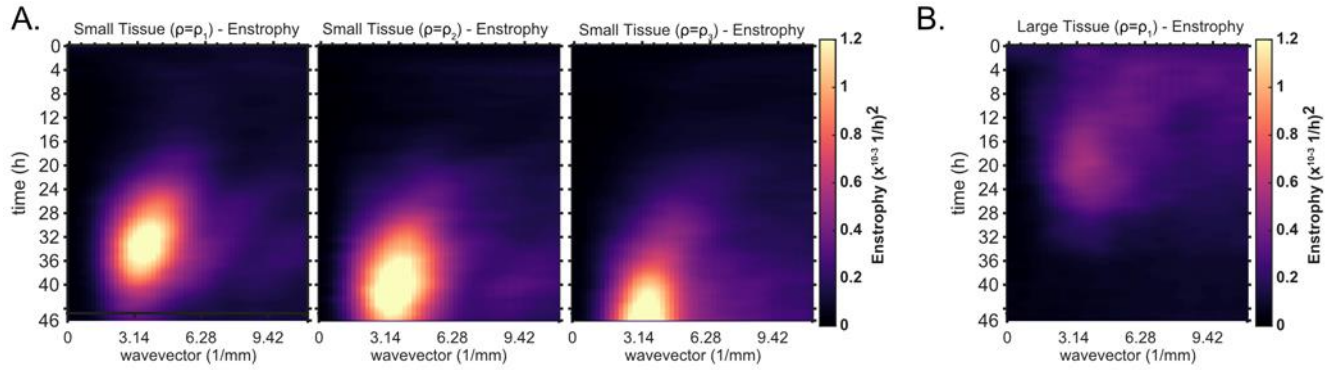

Figure S4. Averaged kymographs of enstrophy, which partition the vorticity power in modes of different wavelengths for each timepoint. (A) From left to right, enstrophy kymographs of small tissues for decreasing starting density. $\rho_1 = [2350,3050]\frac{cells}{mm^2}$, $\rho_2 = [1650,2350)\frac{cells}{mm^2}$, and $\rho_3 = [1300,1650)\ \frac{cells}{mm^2}$. Decreasing starting density clearly delays the onset of high intensity, long wavelength (small wavevector) vorticity. Small tissue enstrophy peaks at a wavevector of ~ 3.14 mm^{-1}, which corresponds to a wavelength of 2 mm. Data from n=16 tissues for $\rho = \rho_1$ (left); n=13 tissues for $\rho = \rho_2$ (middle); and n=11 tissues for $\rho = \rho_3$ (right). (B) Average kymograph of enstrophy for large tissues ($\rho = \rho_1$). The peak at large wavelength is not evident since the vortex is not as prevalent in large tissues.

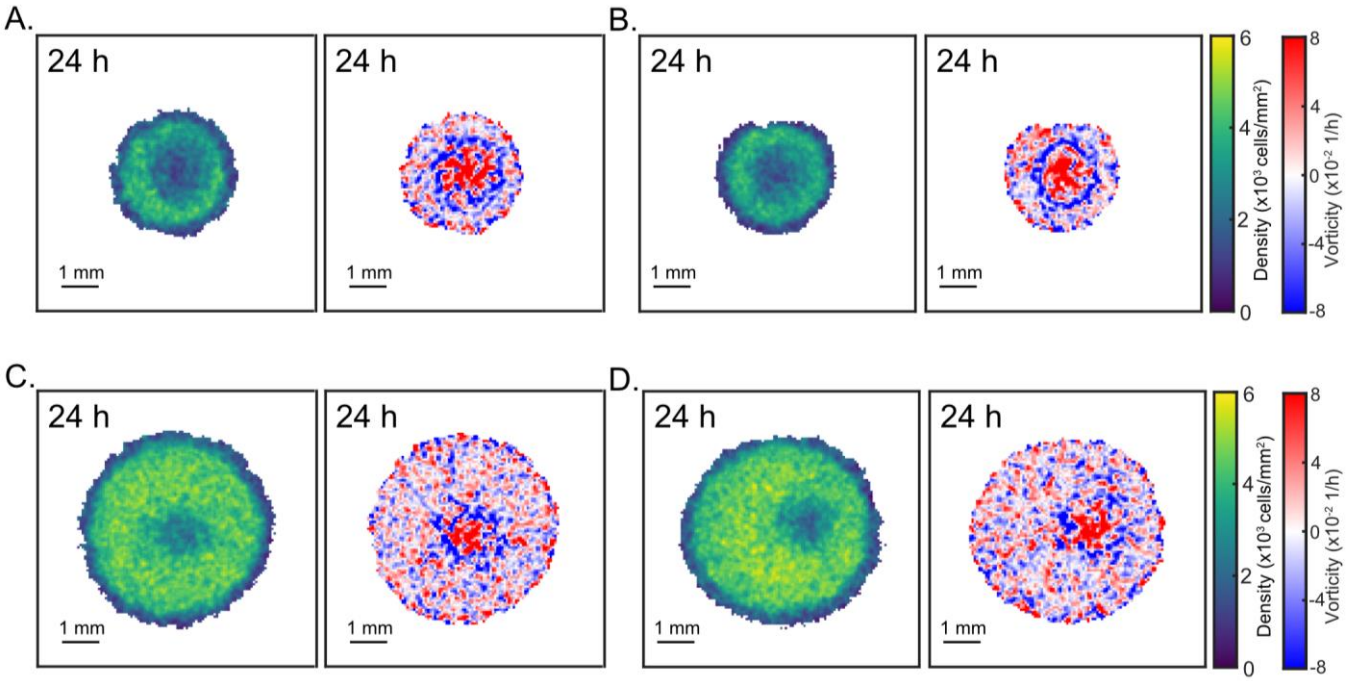

Figure S5. Representative heatmaps of density and vorticity for small tissues and large tissues. A region of low density co-occurs with the vortex in representative small and large tissues, centered and off-centered. Representative tissues include small tissues with vortex/low density region in the center-right (A) and center (B) as well large tissues with vortex/low density region the center (C) and right-of-center (D).

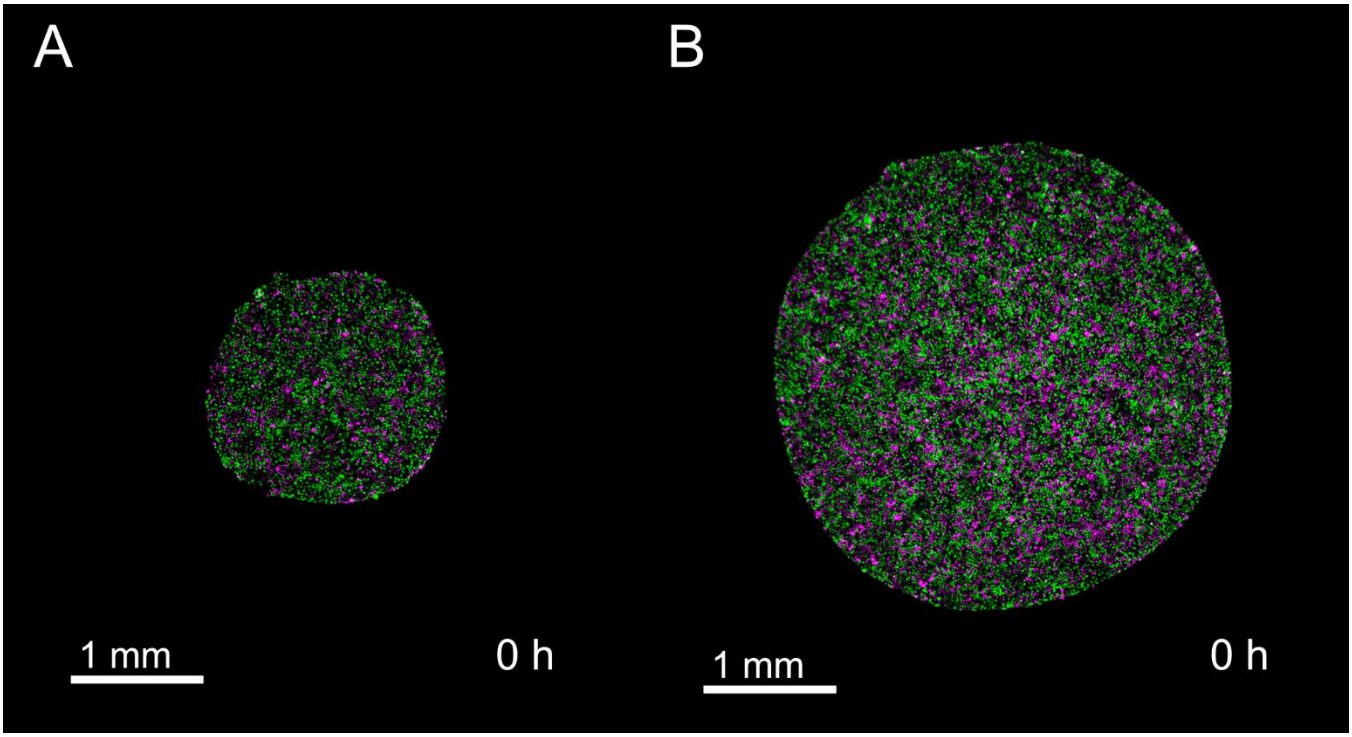

Figure S6. Cells within both small and large tissues are actively cycling at the time of stencil removal. (A) Initial timepoint of representative small tissue. (B) Initial timepoint of representative large tissue.

3. Supplementary Movies

Movie S1. Effect of size on tissue expansion. Time-lapse phase-contrast microscopy of expansion of representative millimeter-size cell monolayers. The movie shows expansion over a 48 hour period for a sample small (left) and sample large (right) tissues.

Movie S2. Time-lapse phase-contrast microscopy showing finger-like protrusions that emerge in the early stages (first 20 hours) of expansion of a cell monolayer.

Movie S3. Effect of aspect ratio on tissue expansion. Time-lapse phase-contrast microscopy of expansion of sample elliptical cell monolayers with varying aspect ratios. Area, cell count, and cell density of each elliptical tissue was matched. The major:minor axis ratio of each ellipse was either 1:1, 4:1, or 8:1.

Movie S4. Vortex formation in a sample small expanding tissue from t=22 hours to 40 hours of expansion. Left panel shows phase-contrast microscopy of an expanding monolayer. Right panel draws the trajectories of individual cells as they evolve through time.

Movie S5. Weak vortex formation in a sample large expanding tissue from t=2 hours to 20 hours of expansion. Left panel shows phase-contrast microscopy of an expanding monolayer. Right panel draws the trajectories of individual cells as they evolve through time.

Movie S6. Coordinated spatiotemporal cell-cycle dynamics in expanding monolayers. Time-lapse fluorescence microscopy of the FUCCI marker for cell-cycle state as the monolayers expand for a small (left) and large (right) tissue over a 48 hour period. Cells in G1 phase are magenta and cells in G2 phase are green.

References

1. S. J. Streichan, C. R. Hoerner, T. Schneidt, D. Holzer, L. Hufnagel, Spatial constraints control cell proliferation in tissues. *Proc. Natl. Acad. Sci.* **111**, 5586–5591 (2014).
2. W. Thielicke, E. Stamhuis, PIVlab--towards user-friendly, affordable and accurate digital particle image velocimetry in MATLAB. *J. Open Res. Softw.* **2** (2014).
3. J. Y. Tinevez, *et al.*, TrackMate: An open and extensible platform for single-particle tracking. *Methods* **115**, 80–90 (2017).
4. Z. Püspöki, M. Storath, D. Sage, M. Unser, We give a methodology-oriented perspective on directional image analysis and rotation-invariant processing. We review the state of the art in the field and make connections with recent mathematical developments in functional analysis and wavelet theory. W. *Focus Bio-Image Informatics*, 69–93 (2016).
5. A. Sakaue-Sawano, *et al.*, Visualizing Spatiotemporal Dynamics of Multicellular Cell-Cycle Progression. *Cell* **132**, 487–498 (2008).